



PCCP

Electronic relaxation dynamics in [Au₂₅(SR)₁₈]-1 (R = CH₃, C₂H₅, C₃H₇, MPA, PET) thiolate-protected nanoclusters

Journal:	<i>Physical Chemistry Chemical Physics</i>
Manuscript ID	CP-ART-07-2019-004039.R1
Article Type:	Paper
Date Submitted by the Author:	30-Jan-2020
Complete List of Authors:	Senanayake, Ravithree ; Kansas State University Aikens, Christine; Kansas State University, Chemistry

SCHOLARONE™
Manuscripts

**Electronic relaxation dynamics in $[\text{Au}_{25}(\text{SR})_{18}]^{-1}$ ($\text{R} = \text{CH}_3, \text{C}_2\text{H}_5, \text{C}_3\text{H}_7, \text{MPA}, \text{PET}$)
thiolate-protected nanoclusters**

*Ravithree D. Senanayake and Christine M. Aikens**

[†]Department of Chemistry, Kansas State University, Manhattan, KS 66506, USA

* cmaikens@ksu.edu, 1-785-532-0954, fax: 1-785-532-6666

Abstract

We investigate the excited electron dynamics in $[\text{Au}_{25}(\text{SR})_{18}]^{-1}$ ($\text{R} = \text{CH}_3, \text{C}_2\text{H}_5, \text{C}_3\text{H}_7, \text{MPA}, \text{PET}$) [MPA = mercaptopropionic acid, PET = phenylethylthiol] nanoparticles to understand how different ligands affect the excited state dynamics in this system. The population dynamics of the core and higher excited states lying in the energy range 0.00–2.20 eV are studied using a surface hopping method with decoherence correction in a real-time DFT approach. All of the ligated clusters follow a similar trend in decay for the core states (S_1 – S_6). The observed time constants are on the picosecond time scale (2–19 ps), which agrees with the experimental time scale, and this study confirms that the time constants observed experimentally could originate from core-to-core transitions and not from core-to-semiring transitions. In the presence of higher excited states, $\text{R} = \text{H}, \text{CH}_3, \text{C}_2\text{H}_5, \text{C}_3\text{H}_7$, and PET demonstrate similar relaxations trends whereas $\text{R} = \text{MPA}$ shows slightly different relaxation of the core states due to a smaller gap between LUMO+1 and LUMO+2 gap in its electronic structure. The S_1 (HOMO \rightarrow LUMO) state gives the slowest decay in all ligated clusters, while S_7 has a relatively long decay. Furthermore, separate electron and hole relaxations were performed on the $[\text{Au}_{25}(\text{SCH}_3)_{18}]^{-1}$ nanocluster to understand how independent electron and hole relaxations contribute to the overall relaxation dynamics.

Introduction

Small thiolate-protected gold clusters in the ~ 2 nm size regime have been identified as promising efficient solar photon harvesters.¹⁻² Their ability to absorb photons in the visible range has been a major reason for their usefulness in photocatalytic applications.¹ Experimental studies have demonstrated that even non-plasmonic clusters such as

$[\text{Au}_{25}(\text{SR})_{18}]^{-1}$ can contribute to photocatalytic enhancement upon visible light irradiation in an Au_{25} -semiconductor system.³⁻⁶ These observations have suggested that the $[\text{Au}_{25}(\text{SR})_{18}]^{-1}$ nanocluster can be a possible photosensitizer in metal cluster-sensitized solar cells.³ Also, $[\text{Au}_{25}(\text{SR})_{18}]^{-1}$ has shown interesting photoluminescence properties⁷⁻¹¹ that are important for future sensing and imaging applications. Therefore, a thorough understanding of the excited state relaxations in $[\text{Au}_{25}(\text{SR})_{18}]^{-1}$ is required for the development of relevant applications.

The $[\text{Au}_{25}(\text{SR})_{18}]^{-1}$ cluster is a well-defined thiolate-protected gold nanoparticle with an icosahedral core that consists of thirteen gold atoms. The gold core is surrounded by six “V-shaped” $-\text{S}-\text{Au}-\text{S}-\text{Au}-\text{S}-$ semiring motifs.¹²⁻¹³ Several different $[\text{Au}_{25}(\text{SR})_{18}]^{-1}$ clusters have been reported experimentally and theoretically depending on the type of the ligand R attached to the sulfur atoms. Some of the SR groups used are alkanethiols such as $-\text{SCH}_3$, $-\text{SCH}_2\text{CH}_3$, $-\text{SC}_6\text{H}_{13}$, $-\text{SCH}_2\text{CH}_2\text{Ph}$; glutathiones; arylthiols such as $-\text{SPhX}$ ($\text{X}=\text{H}$, F, Cl, Br, CH_3 , OCH_3 , NO_2 , *t*Bu); and dithiolates.^{2, 7, 11-25} In the literature, various experimental characterizations of electron relaxation dynamics from excited states lying near the HOMO–LUMO gap and from higher excited states of the $[\text{Au}_{25}(\text{SR})_{18}]^{-1}$ cluster can be found.^{2, 9, 11, 23, 26-29} In these experiments, groups have used different ligands in the R group, including SR = glutathiones, hexanethiols, and phenylethylthiol ($\text{SCH}_2\text{CH}_2\text{Ph}$).

In 2002, Whetten and co-workers performed a femtosecond transient absorption study on the glutathione-stabilized Au_{25} cluster and found two relaxation lifetimes: one around 750 fs and the other on the nanosecond time scale.⁹ Moran and co-workers studied the femtosecond relaxation dynamics of the Au_{25} cluster when the ligand was SR = $\text{SCH}_2\text{CH}_2\text{Ph}$. They proposed a relaxation mechanism involving a relaxation time of ~ 200 fs for the Au_{13} core and a slower 1.2 ps time constant for the relaxation from core to semiring states.¹¹ A femtosecond time-resolved luminescence study of $\text{Au}_{25}\text{L}_{18}$ [L = hexanethiol (C_6S) and glutathione (GS)] by Ramakrishna and co-workers suggested that higher excited state decay constants have lifetimes of 200 fs to a few picoseconds.²⁶ Kamat and co-workers also studied relaxation dynamics of the glutathione-protected Au_{25} nanocluster. In their study, the $\text{Au}_{25}(\text{GS})_{18}$ cluster showed a ~ 1 ps decay constant for a metal-metal transition and a slower ca. 200 ns decay constant for a ligand-to-metal charge transfer.¹ Overall, experimental studies on nonradiative relaxation dynamics on Au_{25}

clusters with different ligand systems have demonstrated varying time constants that span from the femtosecond to nanosecond time scale.

At this point, a systematic theoretical study is needed to explain the different time scales observed for different Au_{25} clusters and provide further insights into the Au_{25} relaxation mechanism. Recent theoretical studies have been performed on understanding the nonradiative excited state relaxations of the $[\text{Au}_{25}(\text{SH})_{18}]^{-1}$ cluster to characterize the electron relaxation dynamics.³⁰⁻³¹ Those investigations considered the smallest possible Au_{25} cluster model with simple SH ligands. In the study by Senanayake et al.,³⁰ the core and higher excited states lying in the energy range of 0.00–2.20 eV were considered in the relaxation dynamics calculations. It was found that relaxations between excited states that arise from core-to-core transitions occur on a short time scale of around 2-18 ps. This study also supported that idea that no semiring states are involved at an energy lower than the core-based S_1 state. The observation suggests that the several picosecond time constants observed by Moran and co-workers could arise from core-to-core transitions rather than from a core-to-semiring transition.³⁰ The SH ligand was used in our previous study to capture the relaxation dynamics of the Au_{25} cluster while reducing the complexity of the geometry of the system and minimizing the computational cost. However, it is important to determine how the trends in the relaxation dynamics differ in the Au_{25} cluster with more realistic ligands. Therefore, an analysis of the relaxation dynamics that occur when the ligands are varied will provide better insight to the relaxation dynamics of the Au_{25} cluster.

Herein, the main goal of this study is to investigate the electronic relaxation dynamics in the thiolate-protected nanocluster series $[\text{Au}_{25}(\text{SR})_{18}]^{-1}$ ($R = \text{CH}_3, \text{C}_2\text{H}_5, \text{C}_3\text{H}_7, \text{MPA}, \text{PET}$) [MPA = mercaptopropionic acid, PET = phenylethylthiol] to understand the ligand effects on relaxation dynamics compared to the $[\text{Au}_{25}(\text{SH})_{18}]^{-1}$ system. The ligands used in this study are closer to common experimentally used ligands such as glutathione and phenylethylthiol that have been used in most of the experimental studies as mentioned above. MPA-ligated gold clusters have been used in a photocatalysis study with TiO_2/gold nanocomposites because MPA has a carboxylic functional group ($-\text{COOH}$) that can covalently bind to the TiO_2 surface.³² Studying the relaxation dynamics of $[\text{Au}_{25}(\text{SR})_{18}]^{-1}$ with different R groups will be beneficial for understanding how the ligands affect the dynamics, especially how the core and the higher excited state relaxations will differ based

on the ligand used. The findings of this investigation will provide better insights into the photophysics of the $[\text{Au}_{25}(\text{SR})_{18}]^{-1}$ nanocluster, which is necessary for its useful applications.

Computational methodology

We have performed ab initio real-time nonadiabatic molecular dynamics (NA-MD) simulations to study the electronic relaxation dynamics in the thiolate-protected nanocluster series $[\text{Au}_{25}(\text{SR})_{18}]^{-1}$ ($\text{R} = \text{CH}_3, \text{C}_2\text{H}_5, \text{C}_3\text{H}_7, \text{MPA}, \text{PET}$; note: in this paper, the abbreviations $\text{R} = \text{MPA}$ and $\text{R} = \text{PET}$ are used to represent the corresponding organic groups attached to the thiol headgroup). The NA-MD simulations were performed using the fewest switches surface hopping (FSSH)³³ algorithm with the classical path approximation and a time-dependent Kohn–Sham description of electronic states (FSSH-TDKS).³⁴ The overcoherent nature of the FSSH approach is corrected by the decoherence-induced surface hopping (DISH)³⁵ scheme. The FSSH simulations are performed using the PYXAID program.³⁶⁻³⁷

The computational methodology has several steps that are described briefly in this section. A detailed explanation of the method employed is given elsewhere.^{30, 36-37} The relaxed geometries of the thiol-protected nanoclusters were obtained by performing a geometry optimization with the PBE³⁸/TZP level of theory with the Amsterdam Density Functional (ADF)³⁹ software package. The zero-order regular approximation (ZORA)⁴⁰ was used to treat the scalar relativistic effects in gold. Linear response time-dependent density functional theory (TD-DFT) calculations were performed using the same level of theory to get the electronic excitations and the absorption spectra.

Secondly, the Vienna Ab initio Simulation Package (VASP)⁴¹ is used to perform temperature ramping and molecular dynamics (MD) calculations. The 0K systems are thermalized through a temperature ramping calculation performed at 300K. An MD trajectory of 5 ps in length was computed with a 1 fs integration time step. We used projector-augmented wave⁴² pseudopotentials, a kinetic energy cutoff value of 402.4 eV for the temperature ramping calculations and a kinetic energy cutoff value of 301.8 eV for the MD simulations and NA coupling calculations (these values are the same as in the previous $\text{R} = \text{SH}$ study), gamma points, and the PBE functional in all of our VASP

calculations. For R = CH₃, C₂H₅, and C₃H₇, a 24 Å simulation box size was used; for MPA, the simulation box size was set to 30 Å due to its larger size. A box size of 34.4 Å x 34.7 Å x 43.6 Å was used for PET. The bigger box sizes for R = MPA and PET will minimize the possible interactions between the neighboring images due to the use of periodic boundary conditions.

In the third step, we calculated the nonadiabatic coupling elements following the same approach described in our previous study on [Au₂₅(SH)₁₈]⁻¹. The NA-MD calculations were performed considering 3.5 ps length sub-trajectories with 10 different starting geometries. For each NA-MD trajectory, 1000 realizations of the stochastic FSSH/DISH state hopping trajectories are considered.

The important electronic excited states contributing to the two main peaks in the optical absorption spectrum of [Au₂₅(SR)₁₈]⁻¹ in the energy range of 0.00–2.20 eV were analyzed both with and without an energy correction to the calculated excited states. With the PBE level of theory, the first excitation peak (S₁-S₆ states) is underestimated by ~0.55 eV compared to the experimental peak. The second peak has a smaller underestimation. Therefore, an excited state energy correction of 0.55 eV was used for the S₁-S₆ states and no correction was used for higher states. The decay times of the excited states populations and the ground state population increase times were calculated for all of the nanoclusters using the following equations and procedure mentioned in our previous study.³⁰

Decay times of the excited state populations:

$$f(t) = \exp\left(-\frac{t}{\tau}\right)$$

Ground state population increase times (GS growth time):

$$f(t) = 1 - \exp\left(-\frac{t}{\tau}\right)$$

For R = CH₃, the MD simulation was performed up to 15 ps where the total MD simulation was considered to consist of three separate simulations (0-5 ps, 5-10 ps and 10-15 ps) and NA coupling and FSSH calculations were carried out to obtain the GS growth and decay time constants for averaging purposes among different simulations. We also carried out a MD simulation starting from a different temperature ramping approach where

TEBEG=0 and TEEND=300 were set in the INCAR file. For the MD simulations from 5-10 ps and 10-15 ps and the simulation with different temperature ramping, the NA couplings were only calculated among orbitals in the range of HOMO-2 to LUMO+1 (accounting for the dynamics of the first absorption peak). The decay time constants were calculated both with and without an energy correction.

Results and discussion

The absorption spectra (Figure 1) calculated for $[\text{Au}_{25}(\text{SR})_{18}]^{-1}$ ($\text{R} = \text{CH}_3, \text{C}_2\text{H}_5, \text{C}_3\text{H}_7, \text{MPA}, \text{PET}$) at the PBE level of theory show strong peaks around similar energies compared to $[\text{Au}_{25}(\text{SH})_{18}]^{-1}$. $[\text{Au}_{25}(\text{SCH}_3)_{18}]^{-1}$ exhibits strong peaks around 1.35 and 2.60 eV. Similarly, the absorption spectra for $[\text{Au}_{25}(\text{SR})_{18}]^{-1}$ ($\text{R} = \text{C}_2\text{H}_5, \text{C}_3\text{H}_7, \text{MPA}, \text{PET}$) display strong peaks around [1.37, 2.60], [1.37, 2.60], [1.30, 2.40], and [1.38, 2.30] eV, respectively. The spectrum for MPA is broader than those for the other four ligands. The peak positions are shifted compared to the three well-defined bands at 1.8, 2.75, and 3.1 eV observed in the $[\text{Au}_{25}(\text{SR})_{18}]^{-1}$ experimental¹²⁻¹³ UV-vis absorption spectrum. The first peak of $[\text{Au}_{25}(\text{SR})_{18}]^{-1}$ with different ligands is redshifted compared to that of $[\text{Au}_{25}(\text{SH})_{18}]^{-1}$. However, the assignment of the first peak in all the clusters (i.e. that it arises from core-to-core transitions within the Au_{13} core between orbitals in the range of HOMO-2 to LUMO+1) studied here is similar to the previous DFT calculations performed on the related $[\text{Au}_{25}(\text{SH})_{18}]^{-1}$ cluster.^{13, 30}

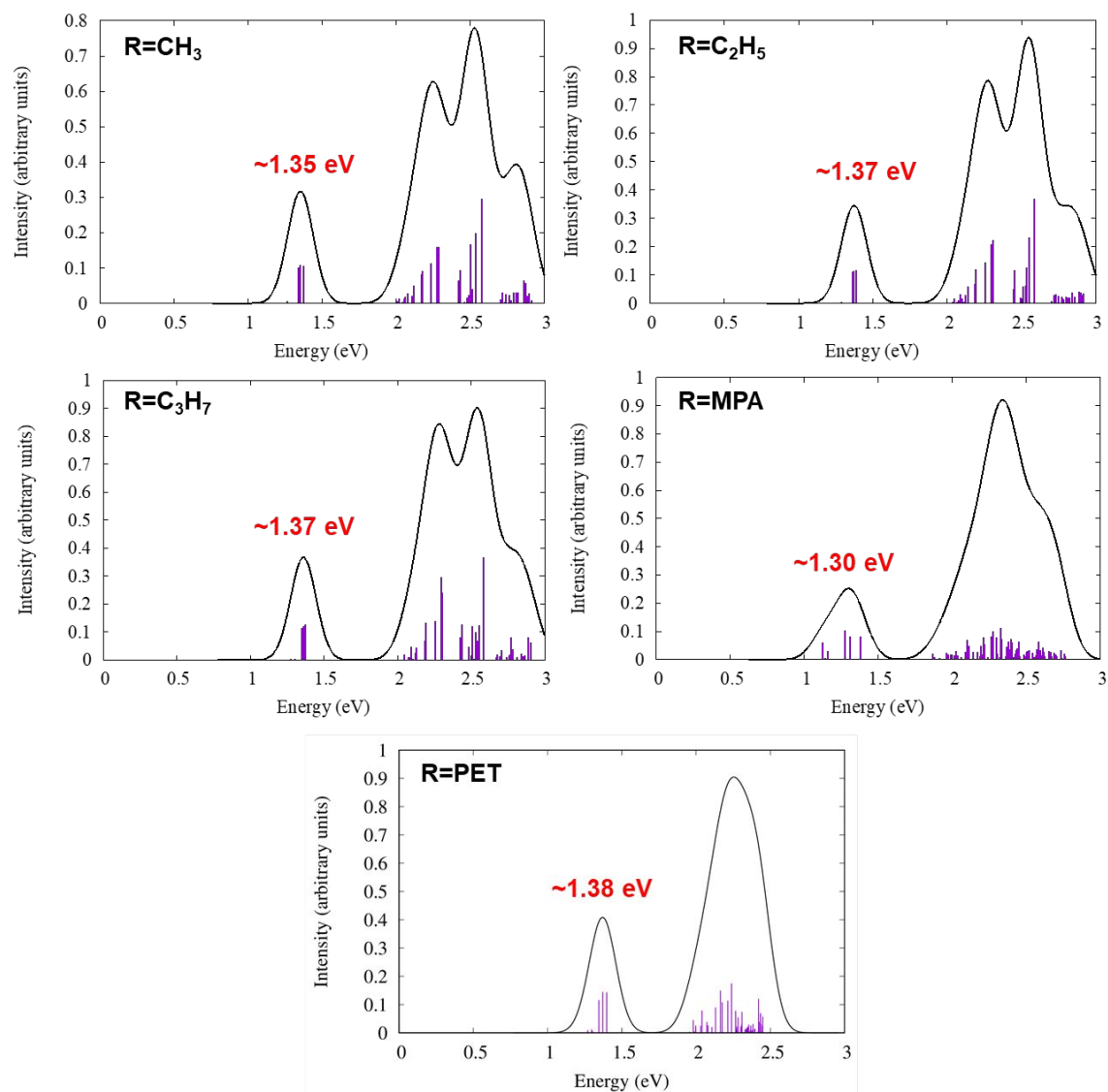


Figure 1. Calculated optical absorption spectra for $[\text{Au}_{25}(\text{SR})_{18}]^{-1}$ ($\text{R} = \text{CH}_3, \text{C}_2\text{H}_5, \text{C}_3\text{H}_7, \text{MPA}, \text{PET}$)

Relaxation dynamics of the first excited state peak in $[\text{Au}_{25}(\text{SR})_{18}]^{-1}$

To understand how electronic relaxation dynamics differ when $[\text{Au}_{25}(\text{SR})_{18}]^{-1}$ is substituted with various ligands R ($\text{R} = \text{CH}_3, \text{C}_2\text{H}_5, \text{C}_3\text{H}_7, \text{MPA}, \text{PET}$), we have studied the first peak in the spectrum that corresponds to the 1.8 eV experimental peak. The first excited state of the clusters with ligands $\text{R} = \text{CH}_3, \text{C}_2\text{H}_5, \text{C}_3\text{H}_7, \text{MPA},$ and PET occurs around 1.35, 1.37, 1.37, 1.30, and 1.38 eV, respectively. The first excited state peak in these four clusters can be attributed to an intraband transition arising from $\text{HOMO} \rightarrow \text{LUMO}$ where the HOMO is nearly triply degenerate and the LUMO is nearly doubly

degenerate as in previously reported theoretical investigations.^{13, 30} In this work, we discuss the approximately doubly degenerate LUMO as two separate orbitals (LUMO and LUMO+1) and the triply degenerate HOMO as three separate orbitals (HOMO, HOMO-1 and HOMO-2) because the near-degeneracy is lifted due to nuclear distortions in the x , y , and z directions during the dynamics. The ~ 1.35 eV peak is constructed primarily from excited states 4, 5, and 6 (Table S1), which have higher oscillator strengths compared to excited states 1 to 3.

Table S1 shows the highest weighted single-particle transitions that contribute to the first peak for the ligated clusters studied in this work. The transitions going from the HOMO, HOMO-1 and HOMO-2 to the LUMO and LUMO+1 are all core-to-core intraband transitions. The transitions responsible for the first peak of the R = MPA cluster are slightly different from the normal trend of transitions shown for other ligated clusters. (More information is given before Table S1 in the Supporting Information.)

We can define the same six excited states for the FSSH-TDKS calculations of the first peak as were defined for the $[\text{Au}_{25}(\text{SH})_{18}]^{-1}$ case (Table 1). These six excited states used in the FSSH-TDKS calculations (Table 1) are slightly different from the first six excited states determined from the TDDFT calculations (Table S1); the FSSH-TDKS calculations use a single Slater determinant while the TDDFT calculations allow for mixed states. In the FSSH-TDKS calculations, the states shown in Table 1 correspond to the six transitions with the highest weights across the first six excited states in the TDDFT calculation.

Table 1. The six excited states considered for the FSSH-TDKS calculations responsible for the first absorption peak. The characterization of the frontier orbitals involved in the corresponding transitions is also shown. Core: orbitals arise primarily in the gold core of the Au_{25} cluster; sp band: orbitals have primarily s and p atomic orbital character from Au.

Excited state	Transition	Characterization of the frontier orbitals (core/semiring assignments)
S ₁	HOMO \rightarrow LUMO	core (sp band) \rightarrow core (sp band)
S ₂	HOMO \rightarrow LUMO+1	core (sp band) \rightarrow core (sp band)
S ₃	HOMO-1 \rightarrow LUMO	core (sp band) \rightarrow core (sp band)

S_4	HOMO-1 \rightarrow LUMO+1	core (<i>sp</i> band) \rightarrow core (<i>sp</i> band)
S_5	HOMO-2 \rightarrow LUMO	core (<i>sp</i> band) \rightarrow core (<i>sp</i> band)
S_6	HOMO-2 \rightarrow LUMO+1	core (<i>sp</i> band) \rightarrow core (<i>sp</i> band)

Clusters with ligands R = CH₃, C₂H₅, C₃H₇, and PET demonstrate near degeneracies of LUMOs and HOMOs similar to [Au₂₅(SH)₁₈]⁻¹. The variation of the orbital energies with time during the MD simulations is shown in Figure 2 for R = CH₃ (R = C₂H₅, C₃H₇, and PET are shown in Figure S1). The orbital energy variation during the MD run for clusters with R = CH₃, C₂H₅, C₃H₇, and PET shows a similar behavior. The HOMO-2, HOMO-1 and HOMO of those clusters are mainly constructed from core gold orbitals (with mixed 6*s* and 6*p* character), whereas the LUMO and LUMO+1 are also constructed of core gold atomic orbitals (with primarily 6*s* character). The lower lying HOMOs are mainly composed from ligand gold (5*d* character) atomic orbitals and from a small amount of sulfur atomic orbitals (3*p* character). Compared to the other ligated Au₂₅ clusters, the electronic structure of the cluster with R = MPA started to indicate a slight difference during the MD simulation (Figure 3). Initially (0–400 fs), the electronic structure exhibits an energy gap between the LUMO+1 and higher level LUMOs; after around 400fs, the energy gap between the LUMO+1 and LUMO+2 decreases. The triple degeneracy of the HOMO, HOMO-1, HOMO-2 is preserved and there is a notable gap between the HOMO-2 and lower level HOMOs for the R = MPA cluster as shown in Figure 3. However, the LUMO orbital energies are closer in energy to each other in the MPA-ligated cluster compared to the other clusters.

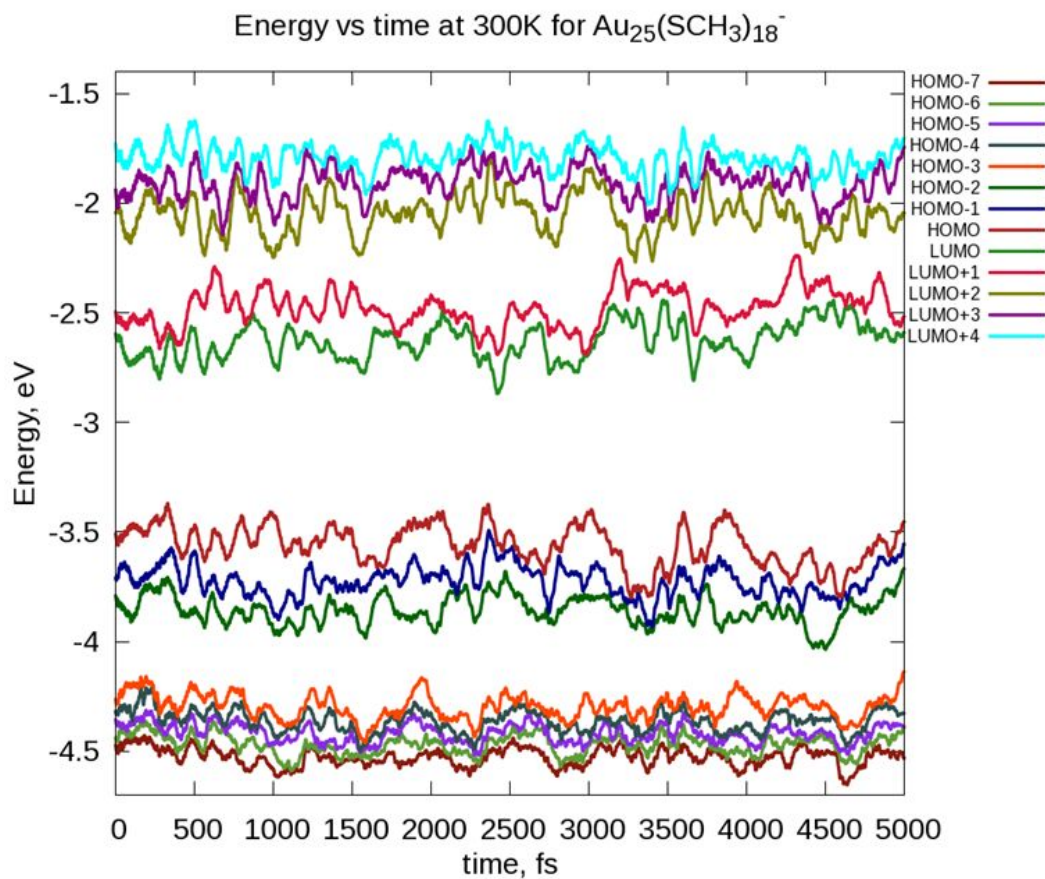


Figure 2. Orbital energy variation with time during the MD simulation for $[\text{Au}_{25}(\text{SCH}_3)_{18}]^-$

1

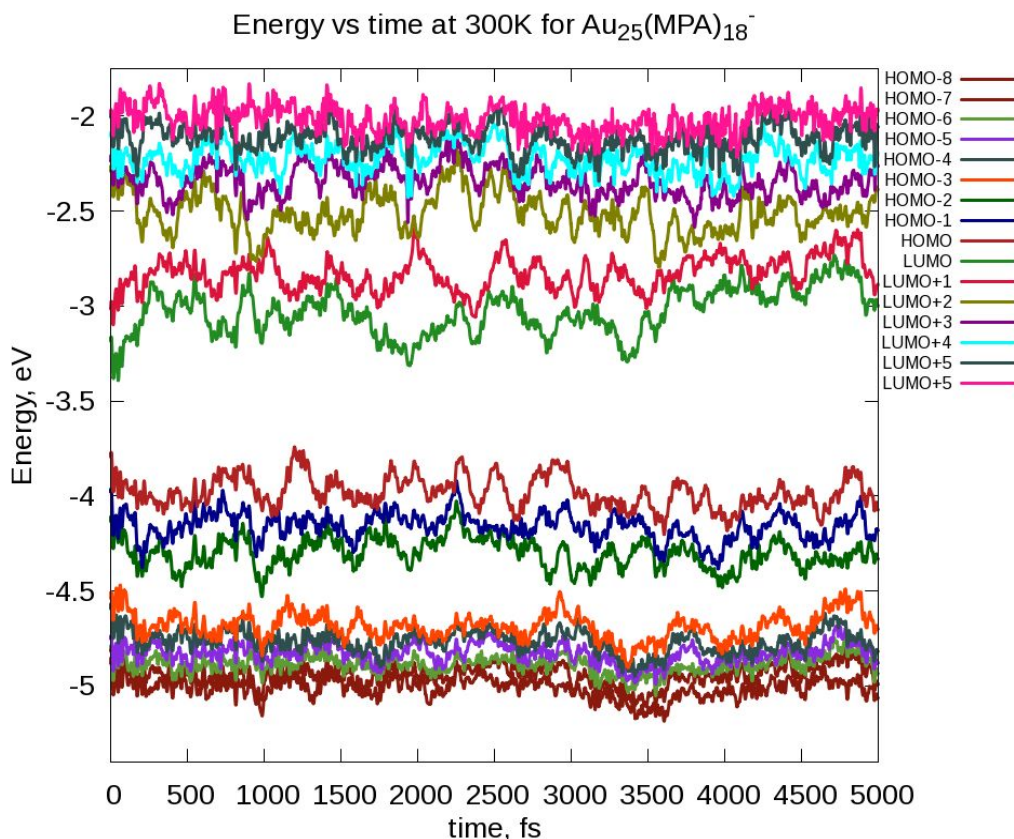


Figure 3. Orbital energy variation with time during the MD simulation for $[\text{Au}_{25}(\text{MPA})_{18}]^{-1}$

Relaxation dynamics of S_1 to S_6 states in $[\text{Au}_{25}(\text{SR})_{18}]^{-1}$

In this section, the electronic relaxation of the first six excited states, S_1 to S_6 , of $[\text{Au}_{25}(\text{SR})_{18}]^{-1}$ with different ligands are discussed. Similar to the $[\text{Au}_{25}(\text{SH})_{18}]^{-1}$ model system studied earlier,³⁰ all six excited states and the ground state (GS) are included in all calculations in this section. The overcoherent nature associated with the FSSH calculation was adjusted by adding decoherence effects through the DISH algorithm implemented in the PYXAID program. Inclusion of the decoherence correction in the calculations changes the decay time values considerably, as shown previously in detail for $[\text{Au}_{25}(\text{SH})_{18}]^{-1}$.³⁰ Therefore, the decoherence correction was added in all calculations discussed in this work. In addition, we also added an energy correction of 0.55 eV to the HOMO-LUMO gap of the various clusters considered in the calculations, to provide a better match with the corresponding experimental value. We used the same 0.55 eV energy correction for the excited states in all clusters due to the similar HOMO-LUMO gaps obtained from the ADF geometry optimizations and to keep the comparison between different clusters consistent.

The relaxation dynamics were performed both “without” and “with” energy corrections to see the implications of this correction on the patterns in the excited state relaxation dynamics in the different clusters. Both the excited state population decays and the GS population increase times are determined in this work.

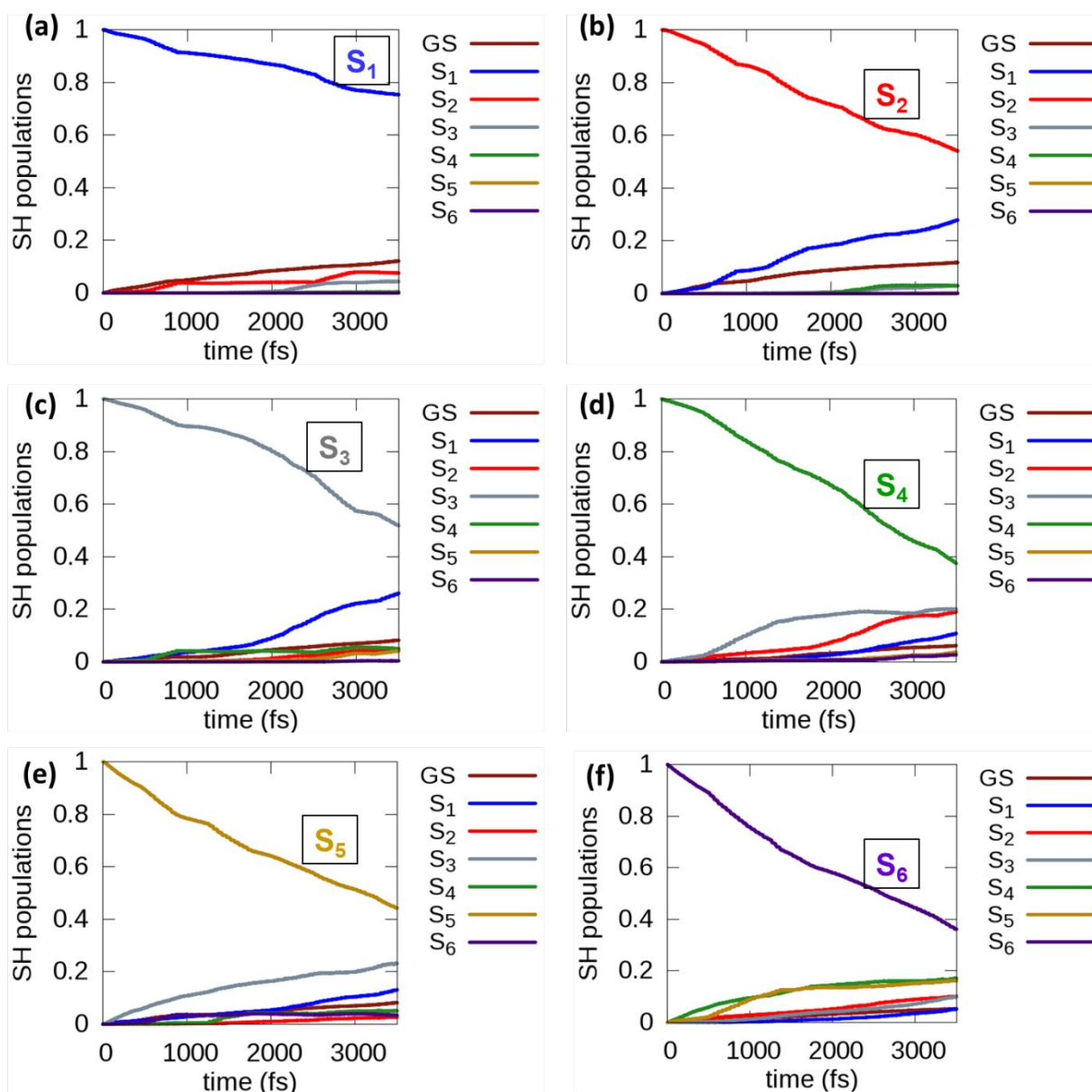


Figure 4. Evolution of the populations of S_1 , S_2 , S_3 , S_4 , S_5 , S_6 states (panels a–f, respectively) for $[\text{Au}_{25}(\text{SCH}_3)_{18}]^{-1}$ without an energy correction

The population dynamics computed without an energy correction for the $[\text{Au}_{25}(\text{SCH}_3)_{18}]^{-1}$ cluster are shown in Figure 4; the relaxation patterns obtained using a 0.55 eV energy correction to the excited states (Figure S2) preserved a similar pattern to those in Figure 4. The relaxation patterns observed for the cluster with the methyl ligand demonstrated a similar relaxation pattern for the S_1 to S_6 state relaxations for $[\text{Au}_{25}(\text{SH})_{18}]^{-1}$.³⁰ The computed GS growth times for the $[\text{Au}_{25}(\text{SCH}_3)_{18}]^{-1}$ cluster are shown in Table 2.

Table 2. Ground state population increase time constants after excitation into the six excited states contributing to the 1.35 eV peak of $[\text{Au}_{25}(\text{SCH}_3)_{18}]^{-1}$

Excited state	GS growth time (ps) without considering the energy correction	GS growth time (ps) with the energy correction
S_1	25	77
S_2	24	105
S_3	43	168
S_4	58	258
S_5	39	215
S_6	62	477

The times for repopulation of the GS increase significantly (by a factor of 3-8) with the addition of the correction, which is logical because the energy gap between the LUMOs and HOMOs has increased; this was also observed for the SH ligand model system.³⁰ The GS growth times are influenced by the presence of intermediate states. For example, a small population of S_1 transfers to the S_2 and S_3 states before relaxing to the GS. The $R = \text{CH}_3$ cluster overall demonstrated shorter GS growth times (24-62 ps seconds without the energy correction) compared to the SH ligand model GS growth times (73-158 ps). The trend in GS growth time constants observed for the first six states follows a similar pattern as in the SH ligand model: states S_1 and S_2 decay to the GS quickly while the other four higher energy states require longer times for repopulation of the GS. Among the S_3 to S_6 states, the S_4 (HOMO-1 \rightarrow LUMO+1) state exhibits the slowest GS growth time when no energy correction is used, whereas S_6 (HOMO-2 \rightarrow LUMO+1) is the slowest with the 0.55 eV energy correction. The results from the GS growth times again confirm that higher

initial excitations lead to slower repopulation to the GS due to the presence of a large number of intermediate states and the higher initial excitation energy. Due to the involvement of the intermediate states, the GS growth is non-exponential, and there is always uncertainty in determining the exact relaxation time constants. However, the approach is useful to get an idea about the relaxation pathways involved.

Table 3. Decay times for the excited state population decrease of the six excited states contributing to the 1.35 eV peak of $[\text{Au}_{25}(\text{SCH}_3)_{18}]^{-1}$

Excited state	Decay time (ps) without considering the energy correction	Decay time (ps) with the energy correction
S_1	13	18
S_2	5.9	7.4
S_3	6.9	7.8
S_4	4.4	4.7
S_5	4.4	4.9
S_6	3.7	3.8

The excited state depopulation time constants are also useful to evaluate as these represent a different process than the GS growth times. $[\text{Au}_{25}(\text{SCH}_3)_{18}]^{-1}$ yields very short decay constants (<20 fs) for all six states both without and with an energy correction (Table 3). Ultrafast decay time constants were also observed for the H ligand model.³⁰ The GS growth time after S_1 state excitation (24 ps) is twice as large as the decay time constant of the S_1 state (12 ps); this occurs because population in the S_1 state can transfer to the S_2 and higher energy states in addition to returning to the ground state. In the H ligand model, this effect was profound where the GS growth time of S_1 was nearly five times larger than the S_1 state decay time.³⁰ In Figure 4a, the S_1 state transfers a small population to S_2 and S_3 and a larger proportion to the GS. When the energy correction is added, a similar degree of population is transferred to the S_2 and S_3 but a slower population growth is observed for the GS. This could further support the idea that S_2 and S_3 states play a vital role in S_1 relaxation.

After initial excitation to the S_2 state, the S_2 state transfers population to S_1 and a small amount of electronic population is transferred to S_4 (Figure 4b). In the H ligand

model, the GS was populated slowly when the S_2 state relaxes,³⁰ whereas with $R = \text{CH}_3$ the GS is populated much faster when the S_2 state relaxes. However, the GS population increase is slower when the energy correction is added as shown in Figure S2b. The excitation of the S_6 state will lead the population to relax into the lower energy S_1 - S_5 states. The populations of the five initially unpopulated excited states reach an average value of ~ 0.1 after the 3.5 ps trajectories, which is less than in the H ligand model case.

To determine error bars for the simulations, the calculated GS growth and decay time constants for states S_1 to S_6 are compared for the initial 5 ps simulation (shown in Tables 2 and 3) with additional MD simulations (from 5-10 ps and 10-15 ps) and for a 5 ps MD simulation started with a different temperature ramping protocol; these values are shown in Table S2. The averages and the standard deviations were calculated considering all four simulations: 0-5 ps, 5-10 ps, 10-15 ps and the simulation with a different temperature ramping protocol (Table S2). The time constants for the FSSH calculations are shown without considering an energy correction. It is important to note that the calculated times constants are sensitive to the nuclear trajectories sampled by the MD simulation. The standard deviations of the GS growth times are much more significant than the standard deviations of the decay time constants. Among the decay time constants, the standard deviations of the S_1 - S_4 states decay are between 1-2.3 ps while S_5 and S_6 have a standard deviation less than 1 ps. We also carried out two different FSSH calculations using the nuclear coordinates and nonadiabatic coupling constants from the 0-5 ps MD simulation; in this case, the S_1 - S_6 GS growth times and excited state decay times were only different in the first decimal point (not shown in the text). This suggests that the 1000 FSSH trajectories themselves for a particular nuclear trajectory are essentially converged, but varying nuclear trajectories can yield different time constants.

$[Au_{25}(SR)_{18}]^{-1} (R = C_2H_5, C_3H_7, MPA, PET)$

Similar to the methyl ligand cluster calculations, relaxation dynamics were performed on ethyl-, propyl-, MPA, and PET-stabilized clusters. The relaxation curves for the clusters with $R = C_2H_5$, C_3H_7 , and PET are shown in the SI (Figures S3, S4, S5, S6, S8, S9) and have similar relaxation patterns as $R = \text{CH}_3$. The curves for $R = \text{MPA}$ without the energy correction are shown in Figure 5.

The ethyl, propyl and PET results show that both S_2 and S_3 could play a role in S_1 state relaxation due to a small amount of population transfer to S_2 and S_3 (Figure S3a, S5a), similar to the methyl ligand. However, in MPA, the S_1 state population primarily transfers to S_3 as shown in Figure 5a and Figure S7.

In ethyl and propyl ligated clusters, the S_6 state population relaxes mainly to the S_4 state. Overall, the S_1 - S_5 states populations reach an average value of ~ 0.15 for ethyl and propyl. In the MPA case, initially the S_6 state relaxes to S_4 and then population later transfers to S_2 , and the S_1 - S_5 states populations eventually reach an average of ~ 0.17 . The S_6 state in PET also relaxes to the S_1 - S_5 states populations and reaches an average of ~ 0.17 .

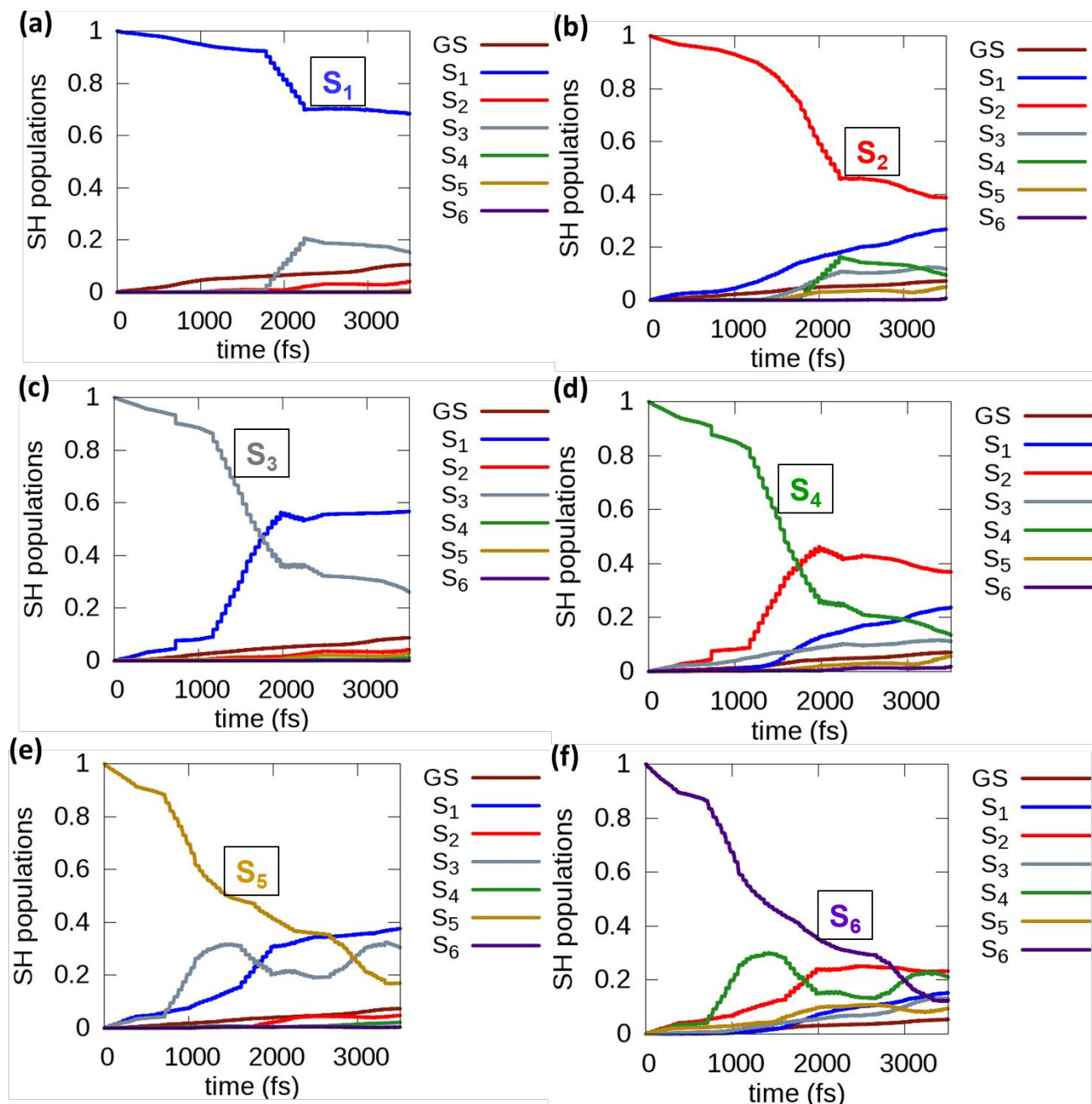


Figure 5. Evolution of the populations of the S_1 , S_2 , S_3 , S_4 , S_5 , S_6 states (panels a-f, respectively) without the energy correction for $[\text{Au}_{25}(\text{MPA})_{18}]^{-1}$.

Compared to the other ligated clusters, the MPA S_1 - S_6 state relaxations show a “step-like relaxation” behavior as shown in Figure 5. In the MPA S_1 state relaxation (Figure 5a), the S_1 population relaxes to S_3 rapidly during the 1900-2400 fs time frame. To understand the relaxation further, we ran separate FSSH calculations on the ten different

initial conditions for the S_1 - S_6 states. The ten initial conditions differ by an offset of 50 fs. All ten relaxations of the S_1 state show a rapid population transfer from S_1 to S_3 at a time corresponding to the 2200-2300 fs time frame of the initial MD run. During the 2200-2300 fs time frame, the HOMO, HOMO-1, and HOMO-2 become close in energy (Figure 3). Moreover, the LUMO and LUMO+1 also become close in energy at the same time. This could facilitate the rapid S_1 state population transfer to the S_3 state because the HOMO and HOMO-1 orbitals are degenerate at that time, so the S_1 and S_3 states are similarly degenerate. A similar explanation can be suggested for the S_3 and S_4 state step-like relaxations, as S_3 (HOMO \rightarrow 1-LUMO) relaxes to the S_1 (HOMO \rightarrow LUMO) and S_4 (HOMO-1 \rightarrow LUMO+1) relaxes to S_2 (HOMO \rightarrow LUMO+1). In both cases, the relaxation occurs during a similar time frame where one can notice the degenerate nature of the HOMO and HOMO-1 orbitals. The degenerate orbitals make the population transfer easier among the states involved.

Comparison of results for different ligands

It is important to note that the GS growth times computed for the ligands R = CH₃, C₂H₅, C₃H₇, MPA, and PET are shorter than the corresponding GS growth times from the SH system (Table 4 and Table S3). This could be due to the presence of the S-C bond and its lower vibrational frequencies in the ligand systems instead of the S-H bond. Due to the complexity in determining the exact relaxation time constants using the GS growth times, we mainly focus on the excited state decay time constants, which are generally invariant to the inclusion of an energy correction to the excited states.

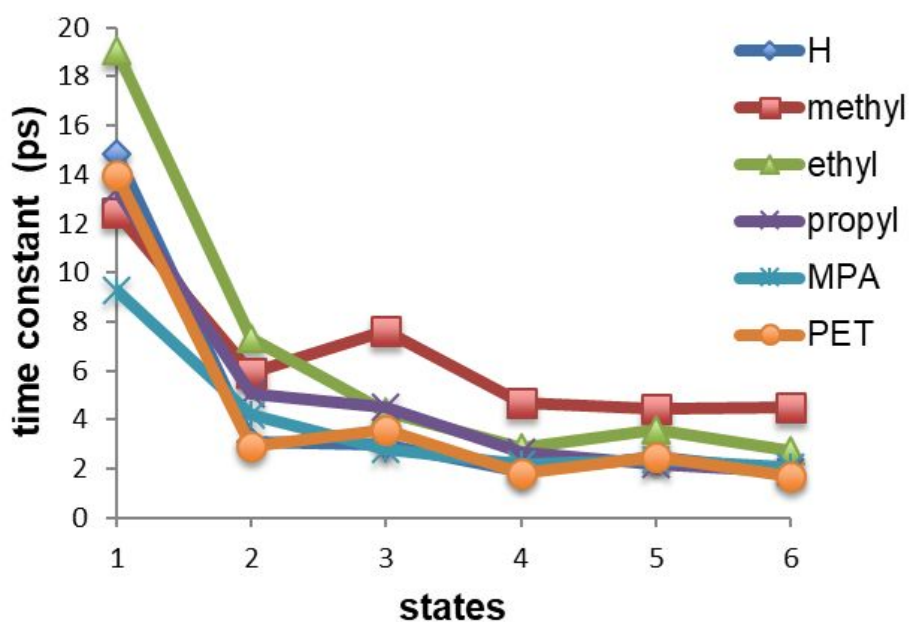
Table 4. GS growth times calculated for ligated clusters. No energy correction is employed.

Excited state	GS growth time (ps)					
	H ³⁰	CH ₃	C ₂ H ₅	C ₃ H ₇	MPA	PET
S ₁	72	24	44	32	30	38
S ₂	71	23	44	34	44	34
S ₃	81	43	50	48	39	34
S ₄	114	55	54	54	49	41
S ₅	95	38	93	37	49	41
S ₆	162	44	83	75	67	68

Table 5 summarizes the excited state decay time constants obtained for all ligated clusters including the H ligand.³⁰ It is important to note that the decay time constants obtained for e.g. the R = MPA S₁-S₆ states may not give the best values due to inherent error in fitting the “step relaxation” populations to an exponential decay. Very short excited state decay times on the picosecond time scale were observed for all ligated clusters; these excited state decay times are much smaller than the corresponding GS growth times. Interestingly, all of the ligated clusters including the H model ligand follow a similar trend of decay time constant variation for the six states as shown in Figure 6. In particular, the decay trend of R = PET is very similar to that of R = H (Figure 6). In ethyl and MPA, the S₃ state does not show an increase in time constant compared to S₂. However, it should be noted that different nuclear trajectories could affect these numbers somewhat; the standard deviation for the methyl ligand for four different nuclear trajectories was approximately 1-2 ps for these states (Table S2). The slowest S₁ state decay time constant is obtained for the ethyl ligand. The decay time constants with the 0.55 eV correction are tabulated in Table S4; the decay times give similar trends both with and without the energy correction.

Table 5. Decay times calculated for the ligated clusters. No energy correction is employed.

Excited state	Decay time (ps)					
	H ³⁰	CH ₃	C ₂ H ₅	C ₃ H ₇	MPA	PET
S ₁	15	12	19	13	9.2	14
S ₂	3.1	5.9	7.3	5.1	4.2	2.9
S ₃	3.0	7.6	4.3	4.5	2.8	3.6
S ₄	1.9	4.7	2.9	2.7	2.2	1.8
S ₅	2.5	4.5	3.6	2.2	2.3	2.5
S ₆	1.9	4.5	2.8	1.9	2.1	1.7

**Figure 6.** Decay time constants for the first six excited states S_N (N=1-6) for thiolate-stabilized gold nanoparticles with different ligands

The ligated clusters studied in this section exhibit a first excited state peak around 1.30 – 1.41 eV in their calculated optical absorption spectra that falls near the energy range of the probe pulse applied in the experimental work (~1.55 – 1.99 eV).¹¹ In the calculations in the current work, the first excited state peak in these ligated clusters arises from core-to-core transitions similar to the previous H ligand³⁰ model. This suggests that the time constants observed experimentally could originate from core-to-core transitions and not from core-to-semiring transitions. The PET ligand was used in the experimental work by

Moran and co-workers.¹¹ Therefore, we can directly compare the decay time constants calculated in our R = PET system with their reported decay for the PET ligand system. The decay constants of the core states (S_1 to S_6) near the HOMO-LUMO gap in the ligated clusters studied in this section are all on the picosecond time scale which agrees well with the experimentally observed¹¹ time constants.

Relaxation dynamics of higher excited states in $[\text{Au}_{25}(\text{SR})_{18}]^{-1}$.

The relaxation dynamics of the higher excited states in the $[\text{Au}_{25}(\text{SR})_{18}]^{-1}$ (R = CH₃, C₂H₅, C₃H₇, MPA, PET) nanoclusters are analyzed in this section. Initial excitations corresponding to the peak around 2.20 eV were considered for all ligated clusters. We performed the analysis by identifying the most probable transitions with the highest oscillator strengths and transition dipole moments. The Au₂₅ clusters with ligands R = CH₃, C₂H₅, C₃H₇, PET have HOMO-7 to LUMO+4 orbitals involved in the main transitions. The Au₂₅ cluster with the MPA ligand yielded HOMO-9 to LUMO+6 orbitals that are involved in the main transitions.

All possible single particle transitions were considered for orbitals between HOMO-7 to LUMO+4 for the clusters with ligands R = CH₃, C₂H₅, C₃H₇, MPA, and PET. Even though the R = MPA cluster can access additional orbitals, we limited our study to transitions involving HOMO-7 to LUMO+4 orbitals for consistency. Therefore, the same excited states are defined for all nanoclusters in the FSSH calculations. These single particle transitions are shown in Table 6 for S_7 - S_{40} ; as before, Table 1 shows the transitions for S_1 - S_6 .

Table 6. Transitions considered for higher excited states. The characterization of the of the frontier orbitals involved in the corresponding transitions are also shown. Core: gold core of the Au₂₅ cluster; semiring: orbitals based on the V-shaped -S-Au-S-Au-S- semirings; *sp* band: orbitals with *s* and *p* atomic orbital character.

Excited state	Transition	Characterization of the frontier orbitals (core/semiring assignments)
S_7	HOMO \rightarrow LUMO+2	core (<i>sp</i> band) \rightarrow core (<i>sp</i> band)/some semiring
S_8	HOMO \rightarrow LUMO+3	core (<i>sp</i> band) \rightarrow core (<i>sp</i> band)/some semiring
S_9	HOMO \rightarrow LUMO+4	core (<i>sp</i> band) \rightarrow core (<i>sp</i> band)/some semiring

S ₁₀	HOMO-1 → LUMO+2	core (<i>sp</i> band) → core (<i>sp</i> band)/some semiring
S ₁₁	HOMO-1 → LUMO+3	core (<i>sp</i> band) → core (<i>sp</i> band)/some semiring
S ₁₂	HOMO-1 → LUMO+4	core (<i>sp</i> band) → core (<i>sp</i> band)/some semiring
S ₁₃	HOMO-2 → LUMO+2	core (<i>sp</i> band) → core (<i>sp</i> band)/some semiring
S ₁₄	HOMO-2 → LUMO+3	core (<i>sp</i> band) → core (<i>sp</i> band)/some semiring
S ₁₅	HOMO-2 → LUMO+4	core (<i>sp</i> band) → core (<i>sp</i> band)/some semiring
S ₁₆	HOMO-3 → LUMO	core (<i>sp</i> band)/semiring → core (<i>sp</i> band)
S ₁₇	HOMO-3 → LUMO+1	core (<i>sp</i> band)/semiring → core (<i>sp</i> band)
S ₁₈	HOMO-3 → LUMO+2	core (<i>sp</i> band)/semiring → core (<i>sp</i> band)/some semiring
S ₁₉	HOMO-3 → LUMO+3	core (<i>sp</i> band)/semiring → core (<i>sp</i> band)/some semiring
S ₂₀	HOMO-3 → LUMO+4	core (<i>sp</i> band)/semiring → core (<i>sp</i> band)/some semiring
S ₂₁	HOMO-4 → LUMO	core (<i>sp</i> band)/semiring → core (<i>sp</i> band)
S ₂₂	HOMO-4 → LUMO+1	core (<i>sp</i> band)/semiring → core (<i>sp</i> band)
S ₂₃	HOMO-4 → LUMO+2	core (<i>sp</i> band)/semiring → core (<i>sp</i> band)/some semiring
S ₂₄	HOMO-4 → LUMO+3	core (<i>sp</i> band)/semiring → core (<i>sp</i> band)/some semiring
S ₂₅	HOMO-4 → LUMO+4	core (<i>sp</i> band)/semiring → core (<i>sp</i> band)/some semiring
S ₂₆	HOMO-5 → LUMO	semiring → core (<i>sp</i> band)
S ₂₇	HOMO-5 → LUMO+1	semiring → core (<i>sp</i> band)
S ₂₈	HOMO-5 → LUMO+2	semiring → core (<i>sp</i> band)/some semiring
S ₂₉	HOMO-5 → LUMO+3	semiring → core (<i>sp</i> band)/some semiring
S ₃₀	HOMO-5 → LUMO+4	semiring → core (<i>sp</i> band)/some semiring
S ₃₁	HOMO-6 → LUMO	semiring → core (<i>sp</i> band)
S ₃₂	HOMO-6 → LUMO+1	semiring → core (<i>sp</i> band)
S ₃₃	HOMO-6 → LUMO+2	semiring → core (<i>sp</i> band)/some semiring
S ₃₄	HOMO-6 → LUMO+3	semiring → core (<i>sp</i> band)/some semiring
S ₃₅	HOMO-6 → LUMO+4	semiring → core (<i>sp</i> band)/some semiring
S ₃₆	HOMO-7 → LUMO	semiring → core (<i>sp</i> band)
S ₃₇	HOMO-7 → LUMO+1	semiring → core (<i>sp</i> band)
S ₃₈	HOMO-7 → LUMO+2	semiring → core (<i>sp</i> band)/some semiring
S ₃₉	HOMO-7 → LUMO+3	semiring → core (<i>sp</i> band)/some semiring
S ₄₀	HOMO-7 → LUMO+4	semiring → core (<i>sp</i> band)/some semiring

The population relaxations of states S₁ to S₆ for the clusters with R = CH₃, C₂H₅, C₃H₇, and PET are shown in the SI (Figures S10, S11, S12, S14). The population relaxations of states S₁ to S₆ exhibit only minor changes when additional higher states are included in the calculations and preserve similar relaxation patterns to those shown in Figures S2, S4, S6, and S9, respectively.

Compared to the decay times from the simulation in which only the S_1 – S_6 states were considered, these states have similar decay times when additional higher excited states are considered for $R = \text{CH}_3, \text{C}_2\text{H}_5, \text{C}_3\text{H}_7,$ and PET (Table S5). Similar to the H model, the S_7 state has a distinctively long lifetime, comparable to that of the S_1 state for the $R = \text{CH}_3, \text{C}_2\text{H}_5, \text{C}_3\text{H}_7, \text{MPA}, \text{PET}$ cases. This likely arises because of a large energy gap between the S_7 and S_6 states, which makes population transfer more difficult. Depopulation of the other higher states ($S_8 - S_{40}$) occurs much faster than that of the S_1 state, on a time scale ranging from 0.4 to 4.1 ps (Table S5), with most decay times predicted to be 1 ps or less.

The decay time constants of S_1 – S_6 are shorter for the $R = \text{MPA}$ cluster compared to the other clusters in the presence of higher excited states (Table S5). With $R = \text{MPA}$, S_1 state population transfers to S_7 which is different from clusters with $R = \text{CH}_3, \text{C}_2\text{H}_5, \text{C}_3\text{H}_7,$ and PET. Furthermore, S_2 state population transfers to S_7 and then to S_1 . The involvement of the S_7 state in S_1 and S_2 relaxations in the $R = \text{MPA}$ cluster could be due to the change in the LUMO orbital energies during the MD run around 400 fs as mentioned earlier. The LUMO orbital energies lie much closer in energy for the MPA cluster compared to the other clusters. The S_1 (HOMO \rightarrow LUMO) population could transfer to S_7 (HOMO \rightarrow LUMO+2) due to the fact that LUMO and LUMO+2 become close in energy as shown by the orbital energy variation in Figure 3. In the presence of the higher excited states, the “step-like relaxation” behavior in the S_1 – S_6 states is less significant (Figure S13). The S_1 – S_6 states become closer in energy to the higher states (S_7 – S_{11}) with the addition of the excited state correction. For example, with only the S_1 – S_6 states present, the S_1 state relaxes to S_3 through a step-like relaxation. In the presence of higher states, the S_1 population transfers to S_7 instead of S_3 . However, the energy difference between S_1 – S_7 is larger than S_1 – S_3 . Therefore, the population transfer $S_1 \rightarrow S_7$ occurs less rapidly than $S_1 \rightarrow S_3$, which results in less “step-like” behavior. For $R = \text{MPA}$ in the presence of higher excited states, the S_7 state gives a relatively slow decay time constant of 8.6 ps whereas the S_1 state yields the slowest decay of 10.7 ps.

Adding the energy correction to the first six states makes the S_1 – S_6 states shift more towards the S_7 . However, in $R = \text{MPA}$ the energy gap between the LUMO+1 and LUMO+2 is less (Figure 3) compared to the other ligand systems considered here. Therefore, the shift

in the S_1 - S_6 states due to the correction is more sensitive in $R = \text{MPA}$ than in the rest of the systems, and the population relaxations reflect this. Thus, we see the S_1 state population transfers mostly to S_7 when the correction is added. This could also be a reason why S_7 has a relatively long decay time constant with the correction. We also performed a relaxation calculation for $R = \text{MPA}$ when no correction is added to the first six states in the presence of the higher excited states. There, we observed a similar trend of decay within the first six excited states. The S_1 decay constant is observed to be 17.4 ps and S_7 now yields a shorter decay constant of 5.1 ps. In the S_1 relaxation, the S_1 population is now mainly transferred to S_2 with only a very small amount transferred to S_7 .

For similar reasons, the $R = \text{PET}$ decay in the presence of higher excited states is calculated without considering a 0.55 eV energy correction for the S_1 - S_6 states as this energy correction will overestimate the energy gaps between the states for the PET system.

Separate electron and hole relaxations in $[\text{Au}_{25}(\text{SCH}_3)_{18}]^{-1}$

In this section we discuss separate electron and hole relaxation dynamics for the $[\text{Au}_{25}(\text{SCH}_3)_{18}]^{-1}$ nanocluster. The analysis was performed to understand how the electrons and holes could relax independently of each other in $[\text{Au}_{25}(\text{SCH}_3)_{18}]^{-1}$. In this calculation, we define the excited states for the FSSH-TDKS calculations (Table S6) in a different order than we defined for the total relaxation dynamics performed in the previous section (Table 1, Table 6).

The S_1 - S_5 states originate by exciting an electron from HOMO to the LUMO-LUMO+4 orbitals, leaving a hole in the HOMO. For clarity, a schematic diagram of orbital levels filled with electrons for the GS and S_1 to S_{40} is shown in Figure 7. We consider the S_1 - S_5 states as one set of electron relaxations (with the same hole). Thus, the forty states (Table S6) can be separated into eight different sets of electron relaxations: S_1 - S_5 , S_6 - S_{10} , S_{11} - S_{15} , S_{16} - S_{20} , S_{21} - S_{25} , S_{26} - S_{30} , S_{31} - S_{35} , and S_{36} - S_{40} . Similarly, the hole relaxations can be separated into five sets. The first set consists of S_1 , S_6 , S_{11} , S_{21} , S_{26} , S_{31} , and S_{36} , in which the electron is excited into the same orbital (LUMO) while leaving a hole in the HOMO, HOMO-1, HOMO-2, ..., and HOMO-7 orbitals, respectively. In the next four hole relaxation sets, the electron is excited into LUMO+1, LUMO+2, LUMO+3, and LUMO+4,

respectively. Separate relaxation calculations were performed for the eight sets of electron relaxations and five sets of hole relaxations.

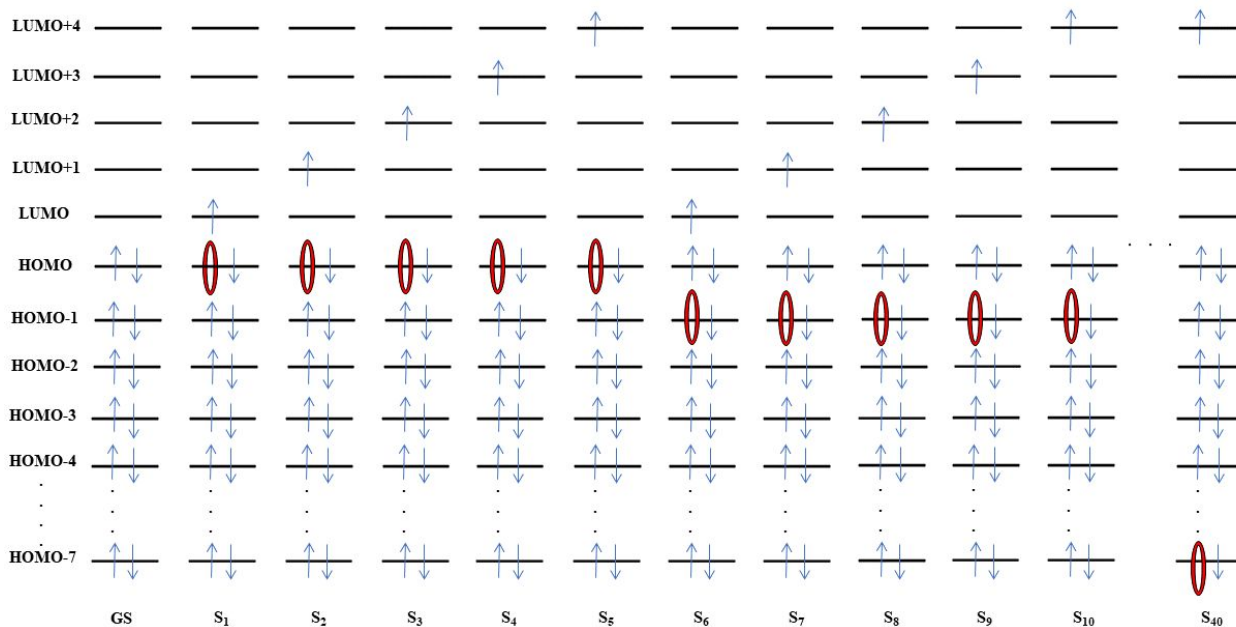


Figure 7. A schematic diagram of orbital levels filled with electrons for GS and S₁ to S₄₀ states considered during the separate electron and hole relaxations.

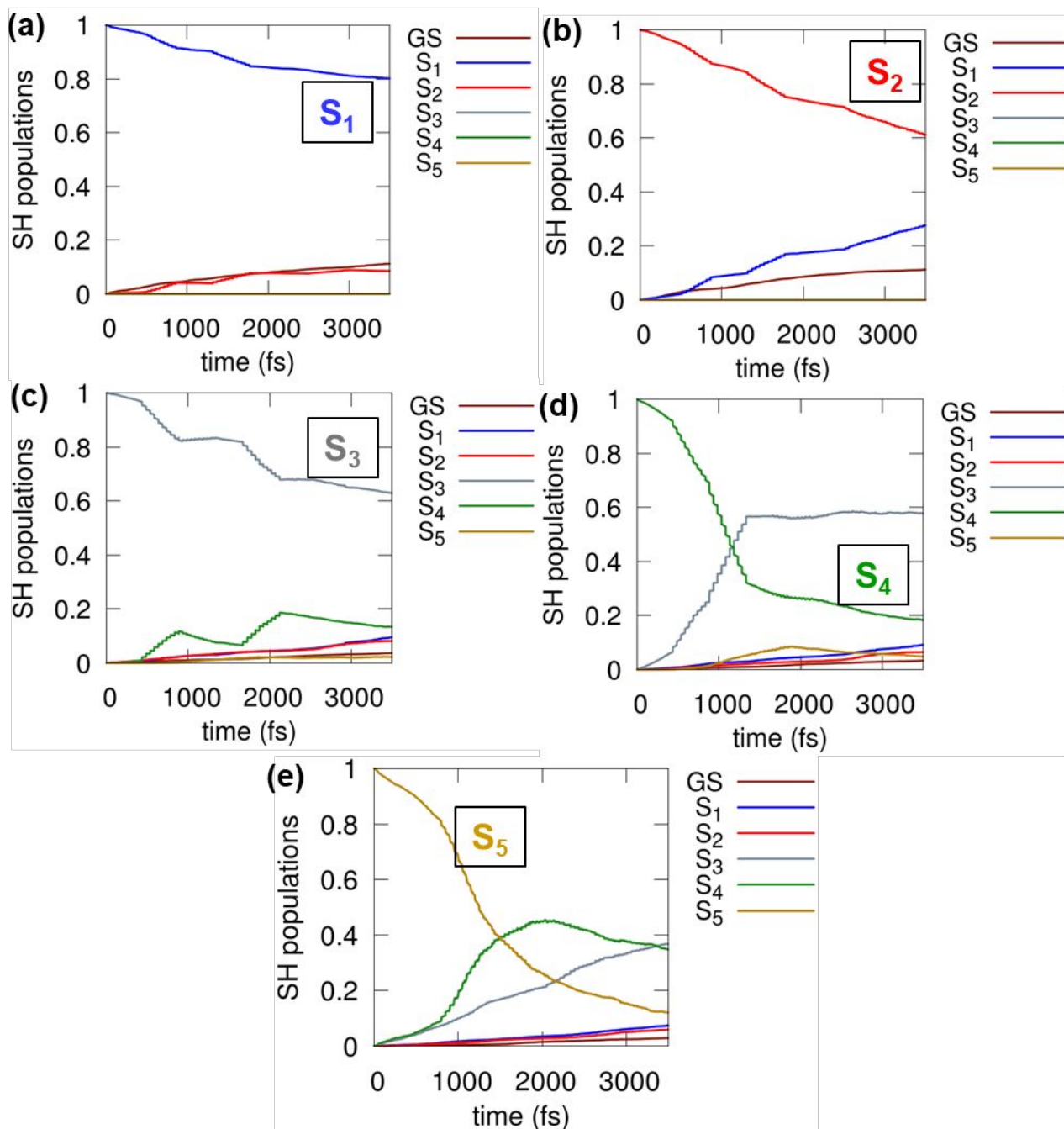


Figure 8. Evolution of the population initially excited into (a) S_1 (b) S_2 (c) S_3 (d) S_4 (e) S_5 during the first set of electron relaxations in $[\text{Au}_{25}(\text{SCH}_3)_{18}]^{-1}$.

The population relaxations of the S_1 - S_5 states in the first set of electron relaxations are shown in Figure 8. Relaxations of states where the electron is excited to the LUMO ($S_1, S_6, S_{11}, S_{16}, S_{21}, S_{26}, S_{31}, S_{36}$) while the hole (Figure S15) is held constant follow similar

population relaxation patterns. Some of the initially excited S_1 population transfers into the higher energy S_2 state (Figure 8a). The S_2 population mainly transfers down to the S_1 state (Figure 8b). This can occur because the LUMO+1 and LUMO lie close in energy. Similar transfer of population from LUMO to LUMO+1 can occur regardless of the hole energy level (Figure S15). One slight difference occurs with repopulation times for the GS. The S_1 state population relaxes to the GS much faster than a higher energy state such as S_{36} relaxes to the GS, which is expected because the S_1 state population can easily transfer to the GS (the electron in the LUMO can fill the hole in the HOMO) whereas it is hard for the S_{36} population to transfer to the GS (the electron in the LUMO would need to fill a hole in the HOMO-7) due to the absence of intermediate states between the S_{36} and GS in this electron-only relaxation. Similar explanations can be given for the remainder of the electron relaxation simulations. Likewise, common population relaxation patterns were observed for the relaxations in which the electron is excited into LUMO+1 through LUMO+4 separately (not shown). The calculated decay constants when the electron is excited into LUMO through LUMO+4 for eight different simulations that differ based on the orbital where the hole is created are plotted in Figure 9 and the values are given in Table S7. All eight electron relaxations follow similar relaxation trends regardless of where the hole is created. Decay constants for states where the electron is initially excited into the LUMO+3 and LUMO+4 orbitals are essentially constant because population transfer from these states is dominated by electron transfer into lower energy LUMOs (see Figure 8d, e). Their decay is faster (short time constants) as they have electron transfer to their nearby intermediate states. The decay from states where the electron is initially excited into LUMO+2 is also constant but with a slow decay due to the population is being mainly transferred to the next higher state (Figure 8c). This could be due to the large energy gap between the LUMO+1 and LUMO+2.

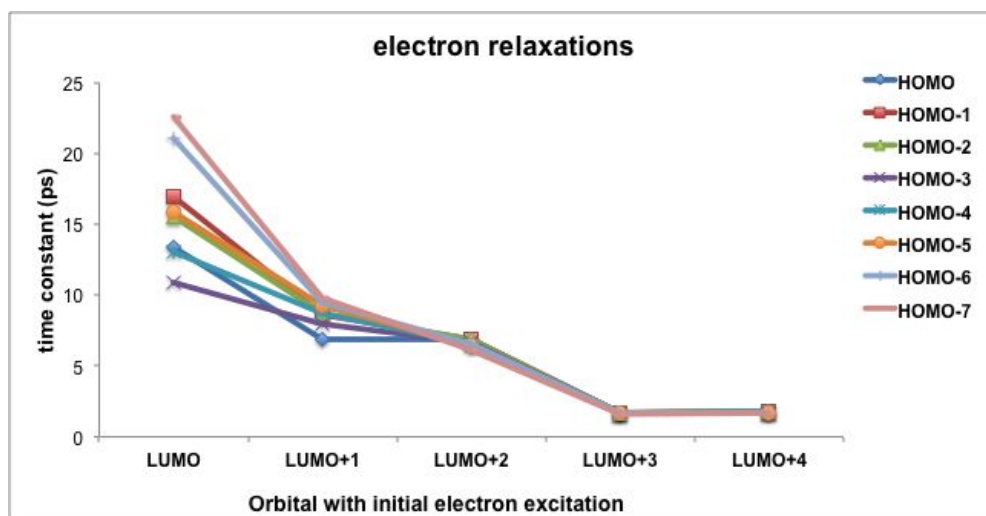


Figure 9. The decay constant trend variation among the five states of each electron relaxation. The legend gives the orbitals where the hole is created for each excitation; the hole is kept constant during each simulation.

Relaxation of the states initially excited into the LUMO is dominated by the energy difference between the LUMO and the HOMO- n orbital. The S_1 state can relax to GS faster while S_6 , S_{11} , S_{16} , S_{21} , S_{26} , S_{31} , and S_{36} cannot relax quickly due to the absence of intermediate states in each electron relaxation set. Thus, they have different time constants. The same principle applies to the states where the electron is excited into LUMO+1. However, the time constants do not vary much compared to each other as they have some intermediate states into which to relax. Therefore, the electron relaxation trend is mainly determined based on their decay into other LUMOs as opposed to decay across the large HOMO(- n)-LUMO gap.

A similar analysis was performed for the hole relaxations. The population relaxations of states where the hole is created in the HOMO follow a similar population relaxation pattern regardless of the orbital into which the electron is excited (Figure S16). Some of the initially excited S_1 population transfers into the higher energy S_6 state (Figure S16). This can occur because the HOMO-1 and HOMO lie close in energy. Similar transfer of population from HOMO to HOMO-1 can occur regardless of the LUMO+ n level occupied by the electron (Figure S16). Analogously, relaxations of states where the hole is created in the HOMO-1 through HOMO-7 have similar relaxation patterns in their population transfer plots (not shown).

For repopulation of the ground state, S_1 and S_2 relax to the GS much faster than states S_3 - S_5 . It is easier for S_1 to relax to the GS than it is for S_3 - S_5 to relax to the GS because an electron in the LUMO has a smaller energy gap for recombination with the hole in the HOMO during a S_1 decay to the GS compared to an electron in the LUMO+2 to LUMO+4 recombining with a hole in the HOMO during a S_3 - S_5 decay to the GS.

Figure 10 and Table S8 give the decay constants for the simulations in which the hole is initially created in HOMO through HOMO-7; these simulations differ based on the orbital into which the electron is excited. The five hole relaxation simulations follow the same trends regardless of where the electron is excited into.

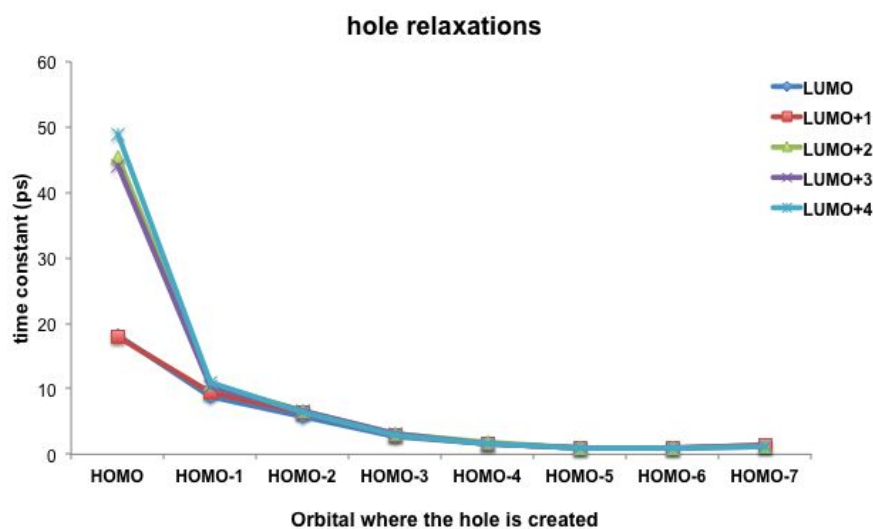


Figure 10. Decay constant trend variation among the eight states for each hole relaxation simulation. The legend gives the orbital where the electron is excited into; this excited electron is kept constant throughout each simulation.

The states where the hole is created in HOMO-3 through HOMO-7 have the same time constants regardless of the orbital into which the electron is excited. For the HOMO-3, the population mainly relaxes into the HOMO-2, HOMO-1, and HOMO and some population is also transferred into the HOMO-4 and HOMO-5 as well. For HOMO-4 to HOMO-7, the main decay pathway is population transfer into the higher energy HOMOs as these represent nearby intermediate states into which they can relax. Due to this reason, the HOMO-3 decay time constants are slightly longer than those for HOMO-4 to HOMO-7.

Thus, the hole relaxation trend for orbitals below the HOMO is decided by their decay into other HOMOs as opposed to decay across the large HOMO-LUMO(+n) gap.

The time constants of states where the hole is created in the HOMO are different from each other. That is, S_1 and S_2 can relax to the GS most quickly, while S_3 - S_5 do not have intermediate states that aid in relaxation. The same applies to the time constants of states where the hole is created in HOMO-1 or HOMO-2. However, their time constants do not vary much since all states have nearby intermediate states to relax.

These calculations were repeated a second time and the decay constants and curves did not change appreciably (Tables S7 and S8). The study confirms that all separate electron relaxations follow a similar trend while separate hole relaxations also follow a common trend.

It is evident that the hole relaxations when the hole is created in HOMO-3 through HOMO-7 are faster than the electron relaxations when the electron is excited into LUMO+2 through LUMO+4. This occurs because the HOMOs below HOMO-3 are denser than the LUMO+2, LUMO+3 and LUMO+4 (Figure 2). However, the electron relaxations when the electron is excited into LUMO or LUMO+1 are comparable to or faster than the hole relaxations when the hole is created in HOMO, HOMO-1 and HOMO-2.

In order to compare the overall dynamics (Table S5) with the separate electron and hole relaxations, we divided the overall dynamics into four sections based on the notable energy gaps between the LUMO+1 and LUMO+2 and between the HOMO-2 and HOMO-3 in the electronic structure. First, the HOMO-LUMO and HOMO-LUMO+1 overall relaxations are similar to the separate electron relaxations. Also, the relaxations of excitations from HOMO-1 and HOMO-2 to LUMO and LUMO+1 have shorter decays compared to the separate electron or hole relaxations. It suggests that the overall dynamics of these states can arise from a mix of electron and hole relaxations. Secondly, relaxations of excitations out of HOMO-HOMO-2 to LUMO+2-LUMO+4 are similar to the respective separate electron relaxations. Next, the relaxations of the excitations out of HOMO-3-HOMO-7 to LUMO-LUMO+1 are similar to the respective separate hole relaxations. Then, the relaxations of the excitations out of HOMO-3-HOMO-7 to LUMO+2-LUMO+4 have shorter decay times compared to the separate electron or hole relaxations. This could be due to the presence of mixed electron-hole relaxations for these states.

Conclusions

The electronic relaxation dynamics in the cluster series, $[\text{Au}_{25}(\text{SR})_{18}]^{-1}$ ($\text{R} = \text{CH}_3, \text{C}_2\text{H}_5, \text{C}_3\text{H}_7, \text{MPA}, \text{PET}$) [MPA = mercaptopropanoic acid, PET = $\text{CH}_2\text{CH}_2\text{Ph}$] were investigated using the FSSH-TDKS method to understand the ligand effects on dynamics. During the MD simulation, the electronic structure of $\text{R} = \text{MPA}$ showed a smaller energy gap between the LUMO+1 and LUMO+2 compared to the rest of the systems including the SH model. For the core states, the GS growth times of the ligand systems are smaller compared to the SH model. All of the ligated clusters including SH follow a similar trend of decay times and the time constants are in range of 2-19 ps for the core states. Relaxation dynamics on the ligated systems further confirm that the time constants observed experimentally could originate from core-to-core transitions and not from core-to-semiring transitions. The observed time constants are on the picosecond time scale which agrees with the experimental time scale.

In the presence of higher excited states, systems with $\text{R} = \text{CH}_3, \text{C}_2\text{H}_5, \text{C}_3\text{H}_7,$ and PET demonstrate similar relaxations in the core states ($\text{S}_1\text{-S}_6$) compared to the case in which only core states were considered. The overall relaxation trend of $\text{R} = \text{CH}_3, \text{C}_2\text{H}_5, \text{C}_3\text{H}_7,$ and PET systems is similar our minimal SH model relaxations where $\text{R} = \text{PET}$ has decay time constants close to the SH model relaxation. In $\text{R} = \text{MPA}$, the relaxations of the core states showed slight differences in the presence of the higher states. The shift in the $\text{S}_1\text{-S}_6$ states by the energy correction could be more sensitive to the relaxations in $\text{R} = \text{MPA}$ than in the rest of the systems due to the small LUMO+1-LUMO+2 gap in its electronic structure. This could be the reason for the involvement of S_7 state in S_1 and S_2 state relaxations for $\text{R} = \text{MPA}$. However, the S_1 state possesses the slowest decay (11-17 ps) while S_7 has a relatively longer decay (8-13 ps) in all ligated clusters.

In $[\text{Au}_{25}(\text{SCH}_3)_{18}]^{-1}$, the electron relaxation trend is decided by the decay of the electron into other LUMOs as opposed to decay across the large HOMO(-n)-LUMO gap, whereas hole relaxation trends are decided by the decay of holes into other HOMOs as opposed to decay across the big HOMO-LUMO(+n) gap. The relaxations of excitations from lower energy HOMOs (HOMO-3 and lower) to core orbitals (LUMO, LUMO+1) are dominated by hole relaxations, and relaxations of excitations from core orbitals (HOMO-

HOMO-2) into higher energy LUMOs (LUMO+2 and above) are dominated by electron relaxations. The remainder of the state relaxations are a mix of both electron and hole relaxations.

Acknowledgments

The work on $[\text{Au}_{25}(\text{SR})_{18}]^{-1}$ (R = CH₃, C₂H₅, C₃H₇) is based on work supported by the National Science Foundation under grant CHE-1507909. This work was performed on the Beocat Research Cluster at Kansas State University, which is funded in part by NSF grants CHE-1726332, CNS-1006860, EPS-1006860, and EPS-0919443, and through the Extreme Science and Engineering Discovery Environment (XSEDE),⁴³ which is supported by National Science Foundation grant number ACI-1053575. Beocat Application Scientist Dr. Dave Turner provided valuable technical expertise. The work on $[\text{Au}_{25}(\text{SR})_{18}]^{-1}$ (R = MPA, PET) used resources of the National Energy Research Scientific Computing Center, a DOE Office of Science User Facility supported by the Office of Science of the U.S. Department of Energy under Contract No. DE-AC02-05CH11231. Research on these two systems is based on work supported by Department of Energy under grant DE-SC0012273. The authors are grateful to Prof. Alexey V. Akimov for his support and valuable discussions on PYXAID.

References

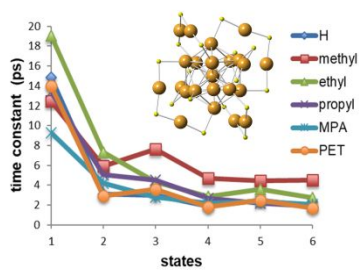
1. Stampelcoskie, K. G.; Kamat, P. V., Size-dependent Excited State Behavior of Glutathione-capped Gold Clusters and Their Light-Harvesting Capacity. *J. Am. Chem. Soc.* **2014**, *136* (31), 11093-11099.
2. Stampelcoskie, K. G.; Chen, Y.-S.; Kamat, P. V., Excited-state Behavior of Luminescent Glutathione-Protected Gold Clusters. *J. Phys. Chem. C* **2014**, *118* (2), 1370-1376.
3. Chen, Y.-S.; Choi, H.; Kamat, P. V., Metal-cluster-sensitized Solar Cells. A New Class of Thiolated Gold Sensitizers Delivering Efficiency Greater than 2%. *J. Am. Chem. Soc.* **2013**, *135* (24), 8822-8825.
4. Kogo, A.; Sakai, N.; Tatsuma, T., Photocatalysis of Au₂₅-modified TiO₂ Under Visible and Near Infrared Light. *Electrochem. Commun.* **2010**, *12* (7), 996-999.
5. Kogo, A.; Sakai, N.; Tatsuma, T., Photoelectrochemical Analysis of Size-dependent Electronic Structures of Gold Clusters Supported on TiO₂. *Nanoscale* **2012**, *4* (14), 4217-4221.

6. Yu, C.; Li, G.; Kumar, S.; Kawasaki, H.; Jin, R., Stable Au₂₅(SR)₁₈/TiO₂ Composite Nanostructure with Enhanced Visible Light Photocatalytic Activity. *J. Phys. Chem. Lett.* **2013**, *4* (17), 2847-2852.
7. Schaaff, T. G.; Whetten, R. L., Giant Gold–Glutathione Cluster Compounds: Intense Optical Activity in Metal-based Transitions. *The Journal of Physical Chemistry B* **2000**, *104* (12), 2630-2641.
8. Link, S.; Beeby, A.; FitzGerald, S.; El-Sayed, M. A.; Schaaff, T. G.; Whetten, R. L., Visible to Infrared Luminescence from a 28-atom Gold Cluster. *The Journal of Physical Chemistry B* **2002**, *106* (13), 3410-3415.
9. Link, S.; El-Sayed, M. A.; Schaaff, T. G.; Whetten, R. L., Transition from Nanoparticle to Molecular Behavior: A Femtosecond Transient Absorption Study of a Size-Selected 28 Atom Gold Cluster. *Chem. Phys. Lett.* **2002**, *356* (3), 240-246.
10. Lee, D.; Donkers, R. L.; Wang, G.; Harper, A. S.; Murray, R. W., Electrochemistry and optical absorbance and luminescence of molecule-like Au₃₈ nanoparticles. *J. Am. Chem. Soc.* **2004**, *126* (19), 6193-6199.
11. Miller, S. A.; Womick, J. M.; Parker, J. F.; Murray, R. W.; Moran, A. M., Femtosecond Relaxation Dynamics of Au₂₅L₁₈⁻ Monolayer-Protected Clusters. *J. Phys. Chem. C* **2009**, *113* (22), 9440-9444.
12. Heaven, M. W.; Dass, A.; White, P. S.; Holt, K. M.; Murray, R. W., Crystal Structure of the Gold Nanoparticle [N(C₈H₁₇)₄][Au₂₅(SCH₂CH₂Ph)₁₈]. *J. Am. Chem. Soc.* **2008**, *130* (12), 3754-3755.
13. Zhu, M.; Aikens, C. M.; Hollander, F. J.; Schatz, G. C.; Jin, R., Correlating the Crystal Structure of a Thiol-protected Au₂₅ Cluster and Optical Properties. *J. Am. Chem. Soc.* **2008**, *130* (18), 5883-5885.
14. Aikens, C. M., Geometric and electronic structure of Au₂₅(SPhX)₁₈⁻ (X= H, F, Cl, Br, CH₃, and OCH₃). *J. Phys. Chem. Lett.* **2010**, *1* (17), 2594-2599.
15. Parker, J. F.; Kacprzak, K. A.; Lopez-Acevedo, O.; Häkkinen, H.; Murray, R. W., Experimental and Density Functional Theory Analysis of Serial Introductions of Electron-Withdrawing Ligands into the Ligand Shell of a Thiolate-Protected Au₂₅ Nanoparticle. *J. Phys. Chem. C* **2010**, *114* (18), 8276-8281.
16. Guo, R.; Murray, R. W., Substituent effects on redox potentials and optical gap energies of molecule-like Au₃₈(SPhX)₂₄ nanoparticles. *J. Am. Chem. Soc.* **2005**, *127* (34), 12140-12143.
17. Akola, J.; Kacprzak, K. A.; Lopez-Acevedo, O.; Walter, M.; Grönbeck, H.; Häkkinen, H., Thiolate-protected Au₂₅ superatoms as building blocks: dimers and crystals. *J. Phys. Chem. C* **2010**, *114* (38), 15986-15994.
18. Jung, J.; Kang, S.; Han, Y.-K., Ligand Effects on the Stability of Thiol-stabilized Gold Nanoclusters: Au₂₅(SR)₁₈⁻, Au₃₈(SR)₂₄, and Au₁₀₂(SR)₄₄. *Nanoscale* **2012**, *4* (14), 4206-4210.
19. Li, G.; Jiang, D.-e.; Liu, C.; Yu, C.; Jin, R., Oxide-supported atomically precise gold nanocluster for catalyzing Sonogashira cross-coupling. *Journal of catalysis* **2013**, *306*, 177-183.
20. Mathew, A.; Natarajan, G.; Lehtovaara, L.; Häkkinen, H.; Kumar, R. M.; Subramanian, V.; Jaleel, A.; Pradeep, T., Supramolecular Functionalization and

- Concomitant Enhancement in Properties of Au₂₅ Clusters. *ACS Nano* **2013**, *8* (1), 139-152.
21. Jupally, V. R.; Kota, R.; Dornshuld, E. V.; Mattern, D. L.; Tschumper, G. S.; Jiang, D.-e.; Dass, A., Interstaple Dithiol Cross-linking in Au₂₅(SR)₁₈ Nanomolecules: A Combined Mass Spectrometric and Computational Study. *J. Am. Chem. Soc.* **2011**, *133* (50), 20258-20266.
22. Dainese, T.; Antonello, S.; Gascón, J. A.; Pan, F.; Perera, N. V.; Ruzzi, M.; Venzo, A.; Zoleo, A.; Rissanen, K.; Maran, F., Au₂₅(SEt)₁₈, a Nearly Naked Thiolate-protected Au₂₅ cluster: Structural Analysis by Single Crystal X-ray Crystallography and Electron Nuclear Double Resonance. *ACS Nano* **2014**, *8* (4), 3904-3912.
23. Stoll, T.; Sgrò, E.; Jarrett, J. W.; Réhault, J.; Oriana, A.; Sala, L.; Branchi, F.; Cerullo, G.; Knappenberger Jr, K. L., Superatom State-resolved Dynamics of the Au₂₅(SC₈H₉)₁₈⁻ Cluster from Two-dimensional Electronic Spectroscopy. *J. Am. Chem. Soc.* **2016**, *138* (6), 1788-1791.
24. Fernando, A.; Weerawardene, K. D. M.; Karimova, N. V.; Aikens, C. M., Quantum Mechanical Studies of Large Metal, Metal Oxide, and Metal Chalcogenide Nanoparticles and Clusters. *Chemical reviews* **2015**, *115* (12), 6112-6216.
25. Jin, R.; Zeng, C.; Zhou, M.; Chen, Y., Atomically Precise Colloidal Metal Nanoclusters and Nanoparticles: Fundamentals and Opportunities. *Chemical reviews* **2016**, *116* (18), 10346-10413.
26. Devadas, M. S.; Kim, J.; Sinn, E.; Lee, D.; Goodson III, T.; Ramakrishna, G., Unique Ultrafast Visible Luminescence in Monolayer-Protected Au₂₅ Clusters. *J. Phys. Chem. C* **2010**, *114* (51), 22417-22423.
27. Green, T. D.; Yi, C.; Zeng, C.; Jin, R.; McGill, S.; Knappenberger, K. L., Temperature-Dependent Photoluminescence of Structurally-Precise Quantum-Confined Au₂₅(SC₈H₉)₁₈ and Au₃₈(SC₁₂H₂₅)₂₄ Metal Nanoparticles. *J. Phys. Chem. A* **2014**, *118* (45), 10611-10621.
28. Yau, S. H.; Varnavski, O.; Goodson III, T., An Ultrafast Look at Au Nanoclusters. *Acc. Chem. Res* **2013**, *46* (7), 1506-1516.
29. Yi, C.; Zheng, H.; Herbert, P. J.; Chen, Y.; Jin, R.; Knappenberger Jr, K. L., Ligand- and Solvent-Dependent Electronic Relaxation Dynamics of Au₂₅(SR)₁₈⁻ Monolayer-Protected Clusters. *J. Phys. Chem. C* **2017**, *121* (44), 24894-24902.
30. Senanayake, R. D.; Akimov, A. V.; Aikens, C. M., Theoretical Investigation of Electron and Nuclear Dynamics in the [Au₂₅(SH)₁₈]⁻¹ Thiolate-Protected Gold Nanocluster. *J. Phys. Chem. C* **2016**, *121* (20), 10653-10662.
31. Chen, X.; Prezhdo, O. V.; Ma, Z.; Hou, T.; Guo, Z.; Li, Y., Ab initio phonon-coupled nonadiabatic relaxation dynamics of [Au₂₅(SH)₁₈]⁻ clusters. *physica status solidi (b)* **2016**, *253* (3), 458-462.
32. Subramanian, V.; Wolf, E. E.; Kamat, P. V., Catalysis with TiO₂/gold Nanocomposites. Effect of Metal Particle Size on the Fermi Level Equilibration. *J. Am. Chem. Soc.* **2004**, *126* (15), 4943-4950.
33. Tully, J., Mixed Quantum-classical Dynamics. *Faraday Discuss.* **1998**, *110*, 407-419.
34. Craig, C. F.; Duncan, W. R.; Prezhdo, O. V., Trajectory Surface Hopping in the Time-dependent Kohn-Sham Approach for Electron-nuclear Dynamics. *Phys. Rev. Lett.* **2005**, *95* (16), 163001.

35. Jaeger, H. M.; Fischer, S.; Prezhdo, O. V., Decoherence-induced Surface Hopping. *J. Chem. Phys.* **2012**, *137* (22), 22A545.
36. Akimov, A. V.; Prezhdo, O. V., The PYXAID Program for Non-adiabatic Molecular Dynamics in Condensed Matter Systems. *J. Chem. Theory Comput.* **2013**, *9* (11), 4959-4972.
37. Akimov, A. V.; Prezhdo, O. V., Advanced Capabilities of the PYXAID Program: Integration Schemes, Decoherence Effects, Multiexcitonic States, and Field-Matter Interaction. *J. Chem. Theory Comput.* **2014**, *10* (2), 789-804.
38. Perdew, J. P.; Burke, K.; Ernzerhof, M., Generalized Gradient Approximation Made Simple. *Phys. Rev. Lett.* **1996**, *77* (18), 3865.
39. Te Velde, G. t.; Bickelhaupt, F. M.; Baerends, E. J.; Fonseca Guerra, C.; van Gisbergen, S. J.; Snijders, J. G.; Ziegler, T., Chemistry with ADF. *J. Comput. Chem.* **2001**, *22* (9), 931-967.
40. Lenthe, E. v.; Baerends, E.-J.; Snijders, J. G., Relativistic Regular Two-Component Hamiltonians. *J. Chem. Phys.* **1993**, *99* (6), 4597-4610.
41. Kresse, G.; Furthmüller, J., Efficiency of Ab-initio Total Energy Calculations for Metals and Semiconductors Using a Plane-wave Basis Set. *Comput. Mater. Sci* **1996**, *6* (1), 15-50.
42. Kresse, G.; Joubert, D., From Ultrasoft Pseudopotentials to the Projector Augmented-wave Method. *Phys. Rev. B* **1999**, *59* (3), 1758.

Table of Contents



Excited state decay times in thiolate-stabilized gold nanoclusters exhibit a degree of dependence on the passivating ligand